Scanning Electrochemical Cell Microscopy (SECCM) in Aprotic Solvents: Practical Considerations and Applications

Cameron L. Bentley,* Minkyung Kang and Patrick R. Unwin

Department of Chemistry, University of Warwick, Coventry CV4 7AL, U.K.

*Corresponding author: c.bentley.1@warwick.ac.uk

ABSTRACT: Many applications in modern electrochemistry, notably electrosynthesis and energy storage/conversion take advantage of the "tunable" physicochemical properties (*e.g.*, proton availability and/or electrochemical stability) of non-aqueous (*e.g.*, aprotic) electrolyte media. This work develops general guidelines pertaining to the use of scanning electrochemical cell microscopy (SECCM) in aprotic solvent electrolyte media to address contemporary structure−electrochemical activity problems. Using the simple outer-sphere $Fc^{0/+}$ process (Fc = ferrocene) as a model system, high boiling point (low vapor pressure) solvents give rise to highly robust and reproducible electrochemistry, whereas volatile (low boiling point) solvents need to be mixed with suitable low melting point supporting electrolytes (*e.g.*, ionic liquids) or high boiling point solvents to avoid complications associated with salt precipitation/crystallization on the scanning (minutes to hours) timescale. When applied to perform microfabrication — specifically the electrosynthesis of the conductive polymer, polypyrrole — the optimized SECCM set up produces highly reproducible arrays of synthesized (electrodeposited) material on a commensurate scale to the employed pipet probe. Applying SECCM to map electrocatalytic activity — specifically the electro-oxidation of iodide at polycrystalline platinum — reveals unique (*i.e.*, structure-dependent) patterns of surface activity, with grains of specific crystallographic orientation, grain boundaries and areas of high local surface misorientation identified as potential electrocatalytic "hot spots". The work herein further cements SECCM as a premier technique for structure−function−activity studies in (electro)materials science and will open up exciting new possibilities through the use of aprotic solvents for rational analysis/design in electrosynthesis, microfabrication, electrochemical energy storage/conversion and beyond.

Surface structure/composition has long been known to have a profound effect on heterogeneous reaction kinetics and/or mechanisms. For instance, in electrochemistry, electrodes of practical importance are often nanostructured to introduce/expose specific sites and/or maximize the active surface area. It follows that understanding the structure−property relationships of functional (electro)materials is of utmost importance, especially with the resurgence of electrochemistry in organic (electro)synthesis and renewable energy storage/conversion technologies.[1] Thus, to complement the ever-expanding library of material nanoengineering strategies,[2] there is a great need for techniques that can probe (electro)chemical activity at the scale of surface heterogeneities, *e.g.*, from single defects (*e.g.*, step edges) and/or nanostructures (*e.g.*, nanoparticles, NPs) to the individual grains and grain boundaries of a polycrystal.[3]

Scanning electrochemical cell microscopy (SECCM) has emerged as a premier technique for correlative structure−function studies in (electro)materials science.[3-5] In SECCM, electrochemical measurements are performed in a statistically-large (typically hundreds to thousands) series of small areas (each nm^2 to μm^2) of a surface, defined by a meniscus cell created between a pipet probe filled with electrolyte solution and substrate (working electrode, WE) surface.[6,7] SECCM probes electrochemistry *directly* at an electrode surface, at a scale commensurate to commonly used structural/compositional characterization techniques (*e.g.*, high-resolution microscopy and/or spectroscopy), allowing structure−activity to be assigned *unambiguously*. Indeed, this innovative correlative electrochemical multi-microscopy approach has previously been applied to resolve the activity of: steps and terraces in layered (two-dimensional) materials;[8-11] individual grains and grain boundaries of polycrystalline metals[12-15] and; single NP or NP agglomerates within an ensemble.[16-18] Complementing these applications, SECCM has also successfully been deployed as a tool for high-throughput fabrication (*i.e.*, electrodeposition) and screening of nanostructured materials at electrode surfaces, notably conductive polymers (CPs)[19,20] and metal NPs.[21,22]

All of the applications of SECCM highlighted above have mainly been carried out in aqueous electrolyte media, where the scanning protocols (*e.g.*, meniscus cell stability, suitable supporting electrolytes and reference electrodes) are well-established.[4,5] Many applications in modern electrochemistry, including the electrosynthesis and energy storage/conversion (*e.g.*, Li-ion batteries and supercapacitors) take advantage of the tunable physicochemical properties of non-aqueous electrolyte media. For example, through careful selection of the solvent and supporting electrolyte, the proton availability, donor/acceptor (*i.e.*, Lewis base/acid) properties, electrochemical stability window *etc.* can be tuned,[23] allowing electrochemical reaction pathways to be controlled to an extent. Although SECCM has previously been applied in aprotic electrolyte media, including in ionic liquids (ILs)[24,25] and organic solvents (and gels),[26,27] the few studies available do not explicitly consider how the solvent/supporting electrolyte affects the stability of the meniscus cell, and the range of solvents studied is quite limited.

Herein, the feasibility of performing SECCM in non-aqueous media, specifically those based on aprotic solvents, is explored

systematically. Taking organic carbonates as a model class of aprotic solvent, general guidelines are established that dictate the choice of solvent/supporting electrolyte to ensure a stable and reproducible electrochemical meniscus cell on the scanning (minutes to hours) timescale. Using the established guidelines, SECCM is applied to perform: (1) local electrodeposition of CP (polypyrrole) arrays and; (2) nanoscale structure–activity mapping of an electrocatalytic process (I^- oxidation). All-in-all, the established guidelines and highlighted applications greatly expand the solvents that can be used in SECCM and further establish it as a robust tool for structure–function studies in (electro)materials science and electroanalytical chemistry.

EXPERIMENTAL SECTION

Chemical reagents and electrode materials. Details in the Supporting Information (SI), Section S1.

Electrochemical measurements. Electrochemical experiments were performed on a home-built SECCM workstation, as previously reported.[4,5,7,28] In this configuration, shown schematically in Figure 1a, a single-barreled pipet probe (fabrication detailed below) was filled with electrolyte solution and mounted on a *z*-piezoelectric positioner (P-753.3, Physik Instrumente, Germany). The WE (nanocrystalline Au or polycrystalline Pt, Figure 1a) was mounted atop an *xy*-piezoelectric positioner (P-621.2, Physik Instrumente). The SECCM probe was initially positioned above the WE using coarse *xy*-micropositioners (M-461-XYZ-M, Newport, U.S.A.), and subsequently lowered into the near-surface position using a stepper motor (8303 Picomotor Actuator, Newport) in tandem with an optical camera (PL-B776U camera, 4× lens, Pixelink, U.S.A.).

The SECCM probe was approached to the WE surface, using a surface current (i_{surf}) threshold of *ca.* 1.5 pA to detect when the meniscus-surface contact had been made and to stop further translation.[6,10,29] Note that the probe itself never made contact with the WE surface. Electrochemical (*i.e.*, amperometry and voltammetry) measurements were performed in the confined area defined by the meniscus cell created between the SECCM probe tip and WE surface. Mapping was carried out using a standard *hopping mode protocol*, as per previous reports.[29,30] In brief, the SECCM probe was approached to the WE surface at a series of predefined locations in a grid (Figure 1a) and, upon each landing, an independent electrochemical measurement was made, building up a spatially-resolved amperometric (i_{surf}–t) or voltammetric (i_{surf}–E) 'image' of the substrate. The final position of the *z*-piezoelectric positioner at approach was also used to build up a topographical map of the substrate (WE), synchronously.

During operation, the SECCM set up was placed on a vibration isolation platform (Minus K, U.S.A.) located within an aluminum faraday cage equipped with heat sinks and acoustic foam. The QRCE potential was controlled, with respect to ground and the current flowing at the WE (*i.e.*, i_{surf}), held at a common ground, was measured using a home-built electrometer. i_{surf} was measured every 4 µs, and averaged in 256 blocks to give a data acquisition rate of 4 × (256 + 1) = 1028 µs (one extra iteration is used to transfer the data to the host computer). Data acquisition and instrumental control was carried out using an FPGA card (PCIe-7852R) controlled by a LabVIEW 2016 (National Instruments, U.S.A.) interface running the Warwick Electrochemical Scanning Probe Microscopy (WEC-SPM, www.warwick.ac.uk/electrochemistry) software.

The single-barreled SECCM probes were fabricated from borosilicate filamented capillaries (GC120F-10, Harvard Apparatus, U.S.A.) using a CO_2-laser puller (P-2000, Sutter Instruments, U.S.A.). The pipet probes were highly reproducible, with tip diameters (d_t) of approximately 200 nm (Figure 1b-i), 750 nm (Figure 1b-ii) or 1.7 µm (Figure 1b-iii), characterized using electron microscopy.[31] Pulling parameters are included in the SI, Section S2. After the SECCM probes were filled with the analyte solution using a MicroFil syringe (World Precision Instruments Inc., U.S.A.), the QRCE (Ag/AgCl or Ag/AgI) was then inserted into the analyte solution, and mounted on the *z*-piezoelectric positioner, ready for use.

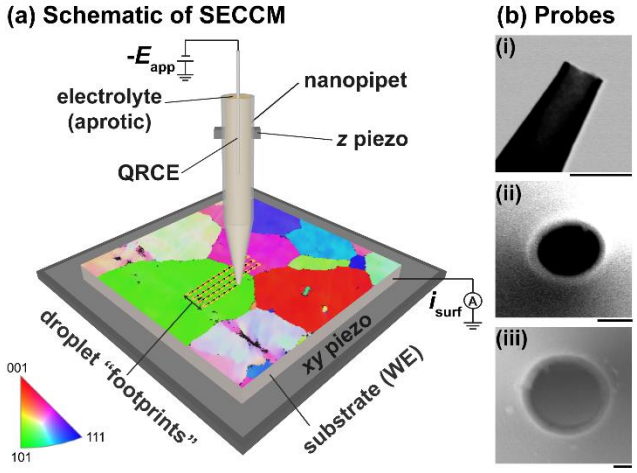

Figure 1. (a) Schematic showing the operation of SECCM in *hopping mode*. A single channel pipet probe, filled with aprotic electrolyte solution, is employed to make local electrochemical measurements at a WE surface (polycrystalline Pt, pictured), by applying a potential ($-E_{app}$) at the QRCE in the probe and measuring the WE (surface) current (i_{surf}). Translation of the probe in 3D (*xyz*) space is achieved using piezoelectric positioners. **(b)** Electron microscopy images of SECCM probes with tip diameters (d_t) of *ca.* **(i)** 200 nm, **(ii)** 750 nm and **(iii)** 1.7 µm. Scale bars indicate 400 nm.

Surface characterization. Details in the SI, Section S1.

Data processing and analysis. Details in the SI, Section S1. Note that all electrochemical/topographical images are presented without any data interpolation.

RESULTS AND DISCUSSION

Selection of solvent and/or supporting electrolyte. The suitability of different solvent/supporting electrolyte combinations for deploying SECCM in aprotic solvent media was the first practical aspect to be explored. In order to do so, the ferrocene/ferrocenium ($Fc^{0/+}$) process was considered:

$$Fc \rightleftharpoons Fc^+ + e^- \quad (1)$$

$Fc^{0/+}$ is known to be a mechanistically simple, outer-sphere process in a range of solvents, characterized by rapid electron-transfer kinetics.[32,33] Indeed, previous SECCM studies (with nanometric pipet probes) have demonstrated that water-soluble Fc derivatives undergo ideal, reversible electron-transfer processes at metal and carbon electrodes.[8,34] Thus, by investigating the $Fc^{0/+}$ process at a topographically flat, uniformly active metallic electrode (nanocrystalline Au, herein), any deviation from ideality was taken as an indicator that the solvent/supporting electrolyte combination was not suitable for SECCM applications.

Linear-sweep voltammograms (LSVs) obtained by averaging 121 independent measurements in the SECCM configuration (d_t ≈ 750 nm, Figure 1b-ii) are shown in Figure 2. Organic carbonates were chosen as "representative" aprotic solvents herein due to their widespread use in Li-ion battery electrolytes.[35] As shown Figure 2a, in propylene carbonate, PC (0.1 M tetra-*n*-butylammonium hexafluorophosphate, [NBu_4][PF_6]) the $Fc^{0/+}$ process is highly reproducible, giving rise to an ideal (Nernstian, *vide infra*) sigmoidal LSV with half-wave potential ($E_{1/2}$) and steady-state limiting current (i_{lim}) values of 0.413 ± 0.002 V *vs* Ag/AgCl quasi-reference counter electrode (QRCE) and *ca.* 15.1 ± 0.2 pA, respectively. Note that a relatively high voltammetric scan rate (υ) of 0.5 V s^{-1} was chosen to allow many measurements to be carried out on a short timescale, in line with previous LSV-SECCM mapping studies.[10,29] Note that the system cannot achieve a true steady-state on this rapid experimental timescale (evidenced by the slightly peak-shaped LSV in Figure 2a, indicative of a transient contribution to mass-transport). Although a true steady-state could be approached through the use of a slower voltammetric scan rate or smaller pipet probes (*vide infra*), previous SECCM studies have shown that non-steady-state effects can be readily accounted for by performing complementary finite element method (FEM) simulations.[6,28] Also note that given the diffusion coefficient of Fc (D_{Fc}) in PC is *ca.* 3 × 10^{-6} cm^2 s^{-1} (Ref 36), i_{lim} is *ca.* 10% of that expected at the same sized microdisk electrode (*ca.* 200 pA), in agreement with previous SECCM reports.[6,28,34]

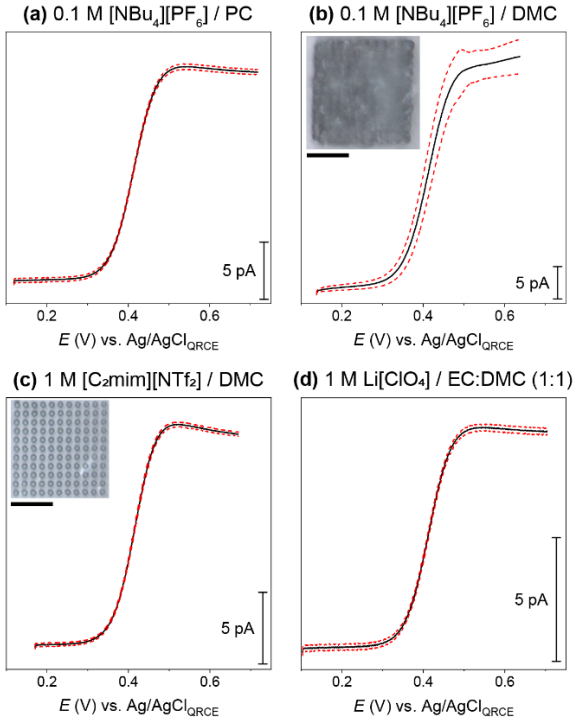

Figure 2. LSVs obtained from the oxidation of 5 mM Fc at a nanocrystalline Au electrode in **(a)** PC (0.1 M [NBu_4][PF_6]), **(b)** DMC (0.1 M [NBu_4][PF_6]), **(c)** DMC (1 M [C_2mim][NTf_2]) and **(d)** 1:1 (w/w) EC:DMC (1 M Li[ClO_4]). Shown on each plot is the average *i*–*E* curve (black trace) ± one standard deviation (red dashed traces), obtained from 121 independent measurements. The LSVs were obtained in the SECCM configuration with d_t ≈ 750 nm (Figure 1b-ii) and voltammetric scan rate (υ) = 0.5 V s^{-1}. Inset in (b) and (c) are OM images taken of the SECCM scan areas, post measurement (scale bar indicates 10 μm).

By contrast, as shown Figure 2b, in dimethyl carbonate, DMC (0.1 M [NBu_4][PF_6]), the $Fc^{0/+}$ process is significantly less reproducible in the SECCM configuration, giving rise to distorted sigmoidal LSVs with $E_{1/2}$ and i_{lim} values of *ca.* 0.41 ± 0.02 V *vs* $Ag/AgCl_{QRCE}$ and *ca.* 36 ± 3 pA. The shape of the average LSV is distorted relative to an ideal case (*e.g.*, Figure 2a), particularly in the mass-transport controlled region (*i.e.*, E > 0.5), which is particularly evident when comparing individual *i*–*E* curves, as shown in the SI, Section S3 (Figure S1). The disparity between the $Fc^{0/+}$ response in DMC and PC is attributed to differences in the electrochemical meniscus cell stability brought on by the precipitation (crystallization) of [NBu_4][PF_6] at the SECCM probe tip during scanning. While this is not usually an issue for SECCM in aqueous media, where supporting electrolyte concentrations of up to 1 M have been reported,[16] DMC is relatively volatile (boiling point, BP = 91°C, vapor pressure (VP) = 55.4 mmHg at 25°C; solvent and supporting electrolyte properties summarized in SI, Section S1, Table S1) compared to water (BP = 100°C, VP = 23.8 mmHg) or PC (BP = 242°C, VP = 0.045 mmHg), and is therefore more prone to local supersaturation (within the meniscus cell) and eventual crystallization of the supporting electrolyte. This was confirmed by optical microscopy (OM), post-experiment (Figure 2b, inset), where the scan area appears to be made up of a solid crystalline mass (*i.e.*, [NBu_4][PF_6]), rather than individual, well-defined droplet footprints.

Aside from using a higher BP solvent (*e.g.*, PC *vs* DMC), another way to avoid the complications illustrated in Figure 2b is to employ a supporting electrolyte that is a room temperature ionic liquid (IL).[25] Shown in Figure 2c is the $Fc^{0/+}$ process in DMC (1 M 1-ethyl-3-methylimidazolium bis(trifluoromethylsulfonyl)imide, [C_2mim][NTf_2]), which is highly reproducible (*i.e.*, comparable to Figure 2a), giving rise to sigmoidal LSVs with $E_{1/2}$ and i_{lim} values of 0.412 ± 0.002 V *vs* $Ag/AgCl_{QRCE}$ and *ca.* 14.5 ± 0.2 pA, respectively. Evidently, changing the supporting electrolyte from crystalline [NBu_4][PF_6] (melting point, MP ≈ 245°C, SI, Table S1) to the IL [C_2mim][NTf_2] (MP ≈ −15°C) stabilizes the SECCM meniscus cell during scanning, confirmed by OM, post-experiment (Figure 2c, inset), where individual well-defined droplet footprints can be seen. Another possibility is to mix the low BP (high VP) solvent with a high BP (low VP) solvent, as is commonplace in Li-ion battery electrolytes, where linear carbonates such as DMC are usually mixed with cyclic carbonates such as ethylene carbonate, EC (BP = 248°C, VP ≈ 0.01 mmHg) to take advantage of the low viscosity of the former and high BP and dielectric constant of the latter.[35] Thus, shown in Figure 2d is the $Fc^{0/+}$ process in a "typical" Li-battery electrolyte, 1:1 (w/w) EC:DMC (1 M Li[ClO_4]). Again, the $Fc^{0/+}$ process is highly-reproducible, giving rise to sigmoidal LSVs with $E_{1/2}$ and i_{lim} values of 0.411 ± 0.002 V *vs* $Ag/AgCl_{QRCE}$ and *ca.* 8.8 ± 0.2 pA, respectively, indicating that the meniscus cell is also stable in this mixed-solvent electrolyte system. It is also worth noting that the i_{lim} values increase in the order 1:1 (w/w) EC:DMC (1 M Li[ClO_4]) < DMC (1 M [C_2mim][NTf_2]) ≈ PC (0.1 M [NBu_4][PF_6]) < DMC (0.1 M [NBu_4][PF_6]), in accordance with the relative viscosities (η) of these electrolytes (SI, Section S1),[35] as per the Stokes-Einstein equation (*i.e.*, $D \propto 1/\eta$).[33,36]

Electrochemical meniscus cell stability on the scanning timescale. The experiments carried out above confirm the viability of various aprotic solvent/supporting electrolyte combinations for SECCM on the minutes timescale (*i.e.*, 121 measurements takes *ca.* 7 minutes), which is on par with the fastest reported

LSV hopping mode scans (≈0.25 s pixel^{-1} or ≈11 minutes for a 2500 pixel scan).[10,29] As "typical" SECCM scans of >1000 pixels are usually on the hours timescale,[5] a larger scan was carried out (4700 measurements over ≈4.5 hours), again considering the $Fc^{0/+}$ process [Eq. (1)] on nanocrystalline Au. Note that PC (0.1 M [NBu_4][PF_6]) has been taken as a "representative" aprotic electrolyte in this and all subsequent SECCM experiments.

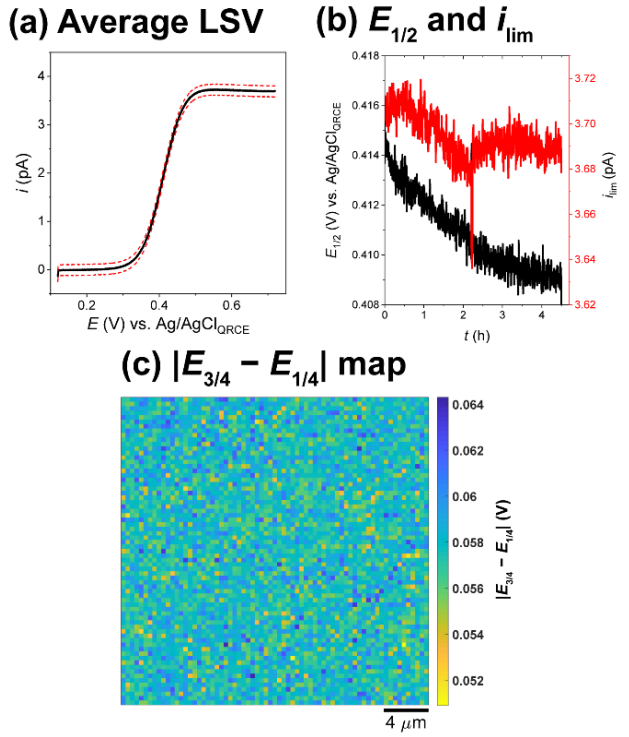

Figure 3. (a) LSV obtained from the oxidation of 5 mM Fc at a nanocrystalline Au electrode in PC (0.1 M [NBu_4][PF_6]). Shown on the plot is the average i–E curve (black trace) ± one standard deviation (red dashed traces), obtained from 4900 independent measurements. The LSVs were obtained in the SECCM configuration with d_t ≈ 200 nm (Figure 1b-i) and υ = 0.5 V s^{-1}. **(b)** Plots of $E_{1/2}$ (black trace) and i_{lim} (red trace) versus scan time (≈4.5 hours, total). **(c)** Spatially-resolved electrochemical map of $|E_{3/4} - E_{1/4}|$ (70 × 70 pixels^2, covering 28 × 28 μm^2 area, hopping distance = 400 nm).

As shown in Figure 3a, the LSVs obtained from the $Fc^{0/+}$ process are highly reproducible on the hours timescale, with $E_{1/2}$ and i_{lim} values of 0.411 ± 0.002 V *vs* Ag/AgCl$_{QRCE}$ and 3.69 ± 0.02 pA, respectively. Note that a smaller SECCM probe (d_t ≈ 200 nm, Figure 1b-i) was employed during this set of experiments, which is why i_{lim} is approximately one quarter of that in Figure 2a (d_t ≈ 750 nm, Figure 1b-ii). Also note that the higher mass-transport rate (≈proportional to $1/d_t$)[6,28] achieved with this smaller probe also results in a sigmoidal LSV that approaches a true steady-state on the experimental timescale (*e.g.*, compare Figures 2a and 3a). As shown in Figure 3b, i_{lim} is relatively unchanged over the ≈4.5 hour scan, while $E_{1/2}$ changes by *ca.* 5 mV from ≈0.414 V to ≈0.409 V. In steady-state voltammetry, a change in $E_{1/2}$ is usually ascribed to differences in electron-transfer kinetics (*i.e.*, a more positive $E_{1/2}$ indicates slower electron-transfer for an oxidation, *vide infra*).[37] In the present case however, the waveshape of the LSV in Figure 3a indicates that $Fc^{0/+}$ process is reversible at all points during the scan, confirmed by calculating the $|E_{3/4} - E_{1/4}|$ values (where $E_{3/4}$ and $E_{1/4}$ are the potentials where $i = 3 \cdot i_{lim}/4$ and $i = i_{lim}/4$, respectively), shown in Figure 3c. Evidently, the $|E_{3/4} - E_{1/4}|$ values satisfy Tomes criterion of reversibility[37] at all points (pixels) within the scan area, with a scan-average value of 58 ± 2 mV (mean ± one standard deviation). Thus, the change in $E_{1/2}$ seen in Figure 3b is attributed to slight drift of the QRCE potential on the order of ≈1 mV hr^{-1}, which is comparable to what has previously been reported for Ag/AgCl QRCEs in aqueous electrolyte media, also in the SECCM configuration.[38]

Application: microfabrication of conducting polymer arrays. Aside from its primary application as a tool for high-resolution electrochemical mapping (*vide infra*),[3,4] the SECCM meniscus "nanocell" configuration can be used for local decoration (*i.e.*, microfabrication) at electrode surfaces.[5] This has been shown to be a particularly powerful approach for the synthesis and screening of three-dimensional (nano)structures, where CPs[19,20] or metal NPs[21,22] are locally electrodeposited and subsequently characterized with high-resolution microscopy to explore the relationship between deposition conditions and material structure/function in a high-throughput manner. In order to explore the viability of this approach in aprotic media, the electropolymerization of pyrrole (Py) to form oxidized polypyrrole (denoted [PPy]$^{n+}$, herein) was explored, shown below in Figure 4. While CPs (*e.g.*, [PPy]$^{n+}$) have found many modern electrochemical applications, for instance as electrodes in sensing[39] and energy storage technologies,[40] the understanding of the interplay between structure/properties (*e.g.*, conductivity) and synthesis conditions is still largely empirical,[41] making high-throughput synthesis/screening strategies invaluable.

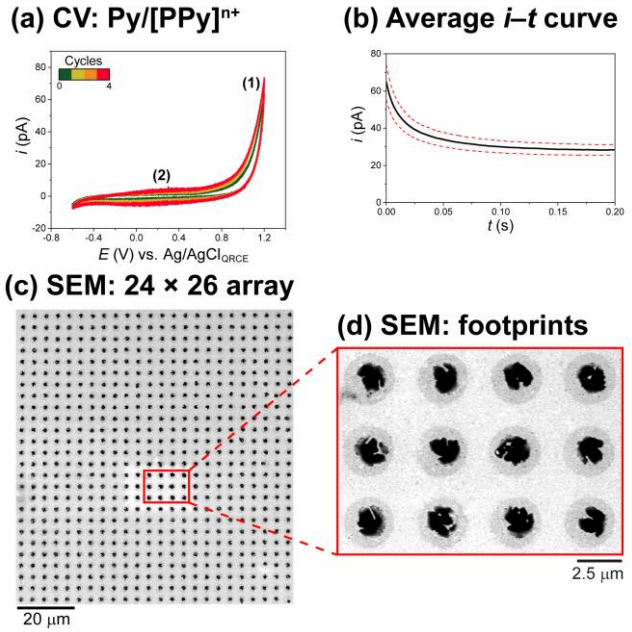

Figure 4. (a) CV (υ = 0.5 V s^{-1}, 4 cycles) and **(b)** i–t curve (E = 1.2 V *vs* Ag/AgCl$_{QRCE}$) obtained from the electropolymerization of Py to [PPy]$^{n+}$ at a nanocrystalline Au electrode. Shown in (b) is the average i–t curve (black trace) ± one standard deviation (red dashed traces), obtained from 624 independent measurements. (a) and (b) were obtained in the SECCM configuration (d_t ≈ 1.7 μm, Figure 1b-iii) in a 10 mM Py in PC (0.1 M [NBu_4][PF_6]) solution. **(c)** SEM image of the 24 × 26 pixel^2 scan area (hopping distance = 5 μm) produced in (b). **(d)** Zoomed in SEM image of the red boxed area in (c), showing the individual droplet footprints.

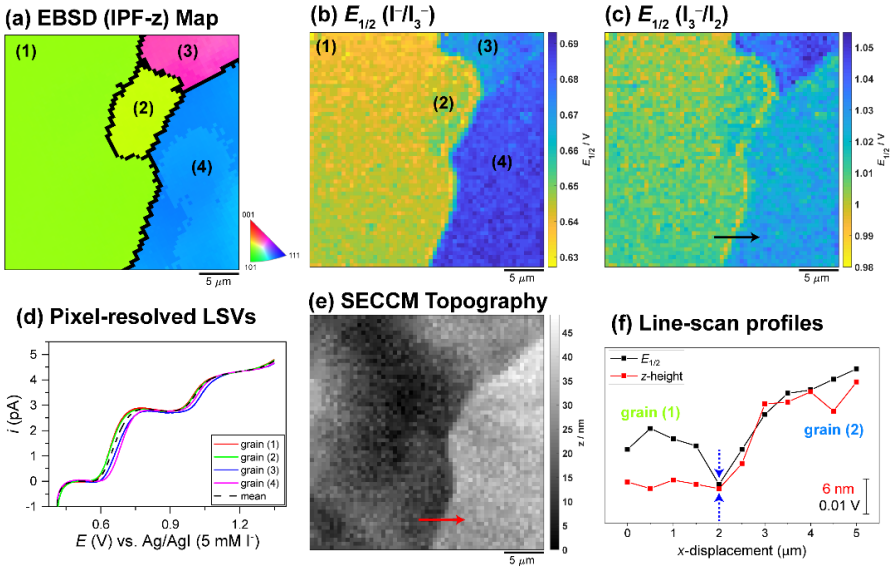

Figure 5. (a) EBSD map of a polycrystalline Pt surface, scanned with SECCM (inverse pole figure, IPF-z indicates surface orientation). **(b – c)** Spatially-resolved $E_{1/2}$ maps (59 × 59 pixels^2 over a 29.5 × 29.5 μm^2 area, hopping distance = 500 nm) for the **(b)** I^-/I_3^- and **(c)** I_3^-/I_2 processes. (b) and (c) were constructed from the *i*–*E* data shown in the SI, Movie S1. **(d)** Pixel-resolved LSVs (υ = 1 V s^{-1}) extracted from grains (1) – (4), labelled in (a) and (b), alongside the area average (dashed black line). **(e)** SECCM topography map, collected synchronously with (b) and (c). **(f)** Line scan profiles of $E_{1/2}$ (I_3^-/I_2) and *z*-height, extracted from the black and red arrows indicated in (c) and (e), respectively. (b – f) were obtained in the SECCM configuration ($d_t \approx 200$ nm, Figure 1b-i) in a 5 mM [NBu$_4$]I in PC (0.1 M [NBu$_4$][PF$_6$]) solution.

Shown in Figure 4a, the cyclic voltammogram (CV) obtained in Py/PC (0.1 M [NBu$_4$][PF$_6$]) solution exhibits two main redox processes, in agreement with previous macroscopic studies[42]: (1) oxidative electropolymerization of Py to $[PPy]^{n+}$ above ≈0.8 V *vs* Ag/AgCl$_{QRCE}$ and; (2) redox cycling (redox switching) of the $[PPy]^{n+}$ film (*i.e.*, $[PPy]^{n+}$/PPy) in the 0 to 0.4 V range. Electropolymerization of a 24 by 26 array of $[PPy]^{n+}$ nanostructures was carried out in the chronoamperometric (constant potential) mode; the average *i*–*t* curve is shown in Figure 4b. For the sake of simplicity, and to check for consistency, the same *E*–*t* waveform (E_{app} = +1.2 V for 200 ms) was applied at all points during the scan. Due to this and the fact that the structure of the nanocrystalline Au electrode is effectively homogeneous on the scale of the SECCM probe ($d_t \approx 1.7$ μm, Figure 1b-iii), the *i*–*t* curves are highly reproducible, with an average charge (*Q*) of 6.5 ± 0.8 pC (proportional to the amount of $[PPy]^{n+}$ deposited) passed during the 200 ms pulse. Note that while a uniform *E*–*t* waveform was applied herein, *E* or *t* can be varied on a per-hop basis to systematically study the interplay between electrodeposition parameters and deposit morphology.[21]

The SEM image of the SECCM scan area, shown in Figure 4c, confirms the reproducibility of the $[PPy]^{n+}$ deposits, which are visible as a rectangular array of uniform black "dots" across the Au electrode surface. Zooming in on an area of the scan, shown in Figure 4d, it is clear that the black $[PPy]^{n+}$ deposits are surrounded by a circular halo, which represents the total area (footprint) wetted by the SECCM meniscus cell during the *E*–*t* pulse (*vide supra*). The diameter of the droplet footprints (*ca.* 2.5 μm, Figure 4d) are comparable to the diameter of the SECCM probe ($d_t \approx 1.7$ μm, Figure 1b-iii), indicating that surface wetting is minimal (wetting ratio, W.R. = $d_{footprint}/d_t \approx 1.5$). Interestingly, while previous SECCM studies in non-aqueous IL-based electrolytes have also demonstrated a stable meniscus cell with minimal surface wetting,[24,25] those carried out in aprotic electrolytes based on PC[27] and dimethyl sulfoxide[26] have shown severe surface wetting, with W.R. values of ≈10 and ≈15, respectively. Evidently, under the conditions investigated herein, the meniscus cell-metal contact is very stable, with scanning spatial-resolution on the order of the tip diameter (*ca.* 200 to 1700 nm, herein, depending on the experiment/application, see Figure 1b), enabling precise electrochemical mapping with high spatial resolution (*vide infra*).

Application: mapping nanoscale structure–activity. As alluded to above, SECCM is primarily employed as a high-resolution electrochemical mapping technique in correlative surface structure–activity studies.[3,4] The feasibility of this approach in aprotic media was explored herein by investigating the electro-oxidation of iodide (I^-) at polycrystalline Pt. I^-/I_2 is a well-known inner-sphere electron-transfer process[43] that proceeds via a one-electron per iodide-ion process on inert electrode materials such as Pt or glassy carbon:

$$2I^- \rightleftharpoons I_2 + 2e^- \quad (2)$$

I^- and I_2 combine homogeneously to form the polyhalogen complex anion, triiodide (I_3^-):

$$I^- + I_2 \rightleftharpoons I_3^- \quad (3)$$

The equilibrium (stability) constant of this reaction is highly solvent dependent, ranging from $\approx 10^{2.9}$ in water to $\approx 10^{7.8}$ in PC, and has a strong bearing on the observed iodide oxidation mechanism.[44] The overall oxidation process shown in Eq. (2) may occur in one step, giving rise to a single voltammetric process (*e.g.*, in water) or in two steps (*via* an I_3^- intermediate), giving rise to two separate voltammetric processes (*e.g.*, in PC):

$$3I^- \rightleftharpoons I_3^- + 2e^- \quad (4)$$

$$I_3^- \rightleftharpoons 3/2\, I_2 + e^- \quad (5)$$

The I^-/I_3^- couple is the most commonly employed redox mediator system in dye-sensitized solar cells (DSSCs), where Eq. (4) takes place (usually) at a platinized counter electrode.[45] More recently, the addition of I^- (in the form LiI) to lithium-oxygen battery electrolytes has been found to reduce the charging overpotential by influencing the cathode product distribution, achieved through the action of the I^-/I_3^- redox mediator sys-

tem.[46] Thus, understanding the surface structure-dependent kinetics/mechanisms of the $I^-/I_3^-/I_2$ redox processes in aprotic media (*e.g.*, PC) is important for the optimization of these devices.

A spatially-resolved electrochemical movie obtained from the oxidation of I^- at polycrystalline Pt is shown in the SI, Movie S1 (caption in the SI, Section S4). Despite the small magnitude of the measured currents (<5 pA), the high signal-to-noise ratio allows the I^-/I_3^- [Eq. (4)] and I_3^-/I_2 [Eq. (5)] processes to be readily distinguished at lower and higher potentials, respectively. Comparison with the EBSD map in Figure 5a reveals that I^-/I_3^- and I_3^-/I_2 are both structure (grain) dependent processes. All of the grains within the scan area [labelled (1) to (4) in Figure 5a] can be described as relatively "high-index", with average crystallographic orientations that are far from the low-index orientations of face-centred cubic (fcc) Pt (*i.e.*, {001}, {011} and {111}). Consulting the spatially-resolved $E_{1/2}$ maps of I^-/I_3^- and I_3^-/I_2, shown in Figure 5b and c, respectively, it is clear that the two processes possess different grain dependencies, with electron-transfer kinetics (inferred from $E_{1/2}$, *vide supra*) decreasing in the order: (1) ≈ (2) > (3) > (4) and (1) ≈ (2) > (4) > (3). These trends are also abundantly clear from the average LSVs extracted from each grain, shown in Figure 5d, which exhibit two processes occurring at potentials of *ca.* 0.7 and 1 V *vs* Ag/AgI (5 mM I^-), corresponding to I^-/I_3^- and I_3^-/I_2, respectively. Interestingly, considering the I^-/I_3^- process in Figure 5d (*i.e.*, process at *ca.* 0.7 V), it is clear that the LSV wave shape/slope is also grain dependent, with $|E_{3/4} - E_{1/4}|$ values of *ca.* 54, 55, 64 and 56 mV for grains (1) to (4), respectively. Note that given $D_{I^-} \approx 3.5 \times 10^{-6}$ cm^2 s^{-1} (Ref 44) and $d_t \approx 200$ nm (Figure 1b-i), i_{lim} (≈5 pA in Figure 5d) is again *ca.* 10% of that expected at the same sized microdisk electrode (*ca.* 60 pA).[28,34] Similar trends in grain-dependent I^- oxidation kinetics were also observed on other areas of the polycrystalline Pt surface, shown in the SI, Movie S2 and Figure S2.

Although the $X^-/X_3^-/X_2$ processes [where X^- is a general halide (Cl^-, Br^- or I^-) or pseudohalide (SCN^- or $SeCN^-$) anion] have been the subject of intensive research in many different solvent media,[44] no consensus has been reached on the electrode reaction mechanism(s). For instance, X_3^- redox has been proposed to occur *via* either direct oxidation/reduction routes [*e.g.*, Eqs. (4) and (5)][47] or generalized *CE* mechanisms [*e.g.*, Eq. (3) followed by Eq. (2)][48] in non-aqueous media. From the different grain dependencies of I^-/I_3^- and I_3^-/I_2 shown in Figure 5b and c, respectively, it may be inferred that the two processes take place preferentially at different active sites, suggesting that the direct oxidation route predominates. Alternatively, the unique structural dependencies of the two processes may result from the potential-dependent specific adsorption of I^-/I_2,[49] which may influence the I^-/I_3^- oxidation sites in a grain-dependent manner.

In addition to the crystallographic orientation of the grains themselves, the I_3^-/I_2 process additionally exhibited enhanced activity in the vicinity of the interface between grains (1)/(2) and (4) (*i.e.*, the grain boundaries). This can be seen by comparing the $E_{1/2}$ (I_3^-/I_2) map (Figure 5c) to the SECCM topographical map (which was collected synchronously with the spatially-resolved electrochemical data), shown in Figure 5e, in which the individual grains can be distinguished topographically, arising from the polishing and flame annealing processes (detailed in the SI, Section S1). Clearly, there is a line of high activity running along the grain boundaries between grains (1)/(2) and (4), visualized by taking line-scan profiles of $E_{1/2}$ and *z*-height, shown in Figure 5e. In the vicinity of the grain boundary (*i.e.*, at *x*-displacement = 2 μm, indicated by blue arrows in Figure 5e), $E_{1/2}$ is shifted negatively by ca. 0.01 V and 0.03 V compared to grains (1) and (4), respectively, indicating enhanced activity towards the I_3^-/I_2 process. Note that similar enhancements in activity towards inner-sphere processes have also been noted in previous SECCM studies,[12-14] but the ability to now perform such studies in aprotic solvent media greatly expands the range of systems that can be mapped with high spatial resolution.

It is also worth noting that in other areas of the polycrystalline Pt surface, non-uniform I^-/I_2 activity was observed within individual grains (*i.e.*, at the intra-grain level). For instance, comparing the electrochemical movie in the SI, Movie S3 to the corresponding EBSD map in Figure 6a, it is clear that the electrochemical activity of grain (1), which makes up >95% of the scan area (labelled in Figure 6a), is non-uniform with regards to both the I^-/I_3^- and I_3^-/I_2 processes. The areas of high electrochemical activity surrounding grains (2) and (3)/(4), particularly for the I_3^-/I_2 process, coincide with regions of grain (1) with relatively high crystallographic misorientation, evident by comparing the misorientation map in Figure 6b [areas labelled (A) and (B)] with the $E_{1/2}$ maps in Figure 6c and d. Note that the misorientation map indicates the local misorientation angle relative to the grain average, with a value ≥10° indicating a grain boundary (indicated by black lines in Figure 6a and b). In the present case, the two areas of relatively high misorientation [*i.e.*, (A) and (B) in Figure 6b] also coincide with local topographical deformation, as shown in the SI, Figure S3. The different patterns of reactivity in Figures 6c and d also imply that the I^-/I_3^- and I_3^-/I_2 processes take place at different active sites on Pt (*vide supra*).

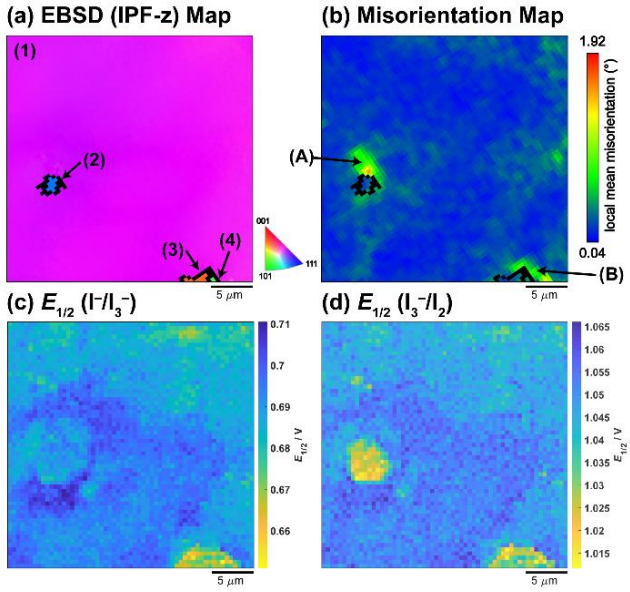

Figure 6. EBSD **(a)** IPF-z and **(b)** misorientation maps of a polycrystalline Pt surface, scanned with SECCM. Individual grains are labelled (1) to (4) in (a). **(c – d)** Spatially-resolved $E_{1/2}$ maps (59 × 59 pixels^2 over a 29.5 × 29.5 μm^2 area, hopping distance = 500 nm) for the **(c)** I^-/I_3^- and **(d)** I_3^-/I_2 processes. (c) and (d) were constructed from the *i*–*E* data shown in the SI, Movie S3. (c) and (d) were obtained in the SECCM configuration ($d_t \approx 200$ nm, Figure 1b-i) in a 5 mM $[NBu_4]I$ in PC (0.1 M $[NBu_4][PF_6]$) solution.

CONCLUSIONS

Taking organic carbonates as a model class of aprotic solvent, SECCM was successfully adapted to operate in non-aqueous

electrolyte media. Investigating the simple outer-sphere $Fc^{0/+}$ process, it was shown that high BP (low VP) solvents (*e.g.*, PC) give rise to robust and reproducible electrochemistry on the scanning (hours) timescale, while low BP (high VP) solvents (*e.g.*, DMC) need to be combined with suitable low MP supporting electrolytes (*e.g.*, ILs) or high BP solvents (*e.g.*, EC) to avoid complications associated with salt precipitation/crystallization. SECCM was applied for microfabrication, by synthesizing (depositing) a microarray of $[PPy]^{n+}$ on a nanocrystalline Au electrode surface, which was subsequently characterized with SEM to confirm the reproducibility of the technique and stability of the meniscus cell during scanning. Finally, high-resolution electrochemical mapping of the I^-/I_3^- and I_3^-/I_2 processes across the surface of a polycrystalline Pt electrode revealed unique, structure-dependent patterns of surface reactivity at for example, individual grains, grain boundaries and areas of high local surface misorientation. Overall, this study expands SECCM as a premier technique for structure−function−activity studies in (electro)materials science, opening up possibilities in exciting new areas such as the microfabrication of water-sensitive materials (*e.g.*, electrodeposition of reactive metals, which will be facilitated by housing SECCM in a glovebox) or electrochemical mapping of processes relevant to electrochemical energy storage (*e.g.*, Li-ion batteries and supercapacitors) and electrocatalysis.

ASSOCIATED CONTENT

Supporting Information

The Supporting Information (SI) is available free of charge on the ACS Publications website.

Supplementary experimental section (Section S1), pipet pulling parameters (S2), additional experimental data (S3) and movie captions (S4), as described in the main text (PDF)

Electrochemical movie showing the electro-oxidation of I^- at polycrystalline Pt, Movies S1 (AVI), S2 (AVI) and S3 (AVI)

AUTHOR INFORMATION

Corresponding Author

*E-mail: c.bentley.1@warwick.ac.uk

ACKNOWLEDGMENT

C.L.B. acknowledges financial support from the Ramsay Memorial Fellowship Trust. M.K. was supported by the Monash−Warwick Alliance Accelerator fund. P.R.U. gratefully acknowledges support from a Royal Society Wolfson Research Merit Award. We also thank the EPSRC Faraday Challenge Battery Characterisation Challenge (FIRG013) for support.

REFERENCES

(1) Seh, Z. W.; Kibsgaard, J.; Dickens, C. F.; Chorkendorff, I.; Nørskov, J. K.; Jaramillo, T. F. Combining Theory and Experiment in Electrocatalysis: Insights into Materials Design. *Science* **2017**, *355*, 146.

(2) Li, F.; MacFarlane, D. R.; Zhang, J. Recent advances in the nanoengineering of electrocatalysts for CO2 reduction. *Nanoscale* **2018**, *10*, 6235-6260.

(3) Bentley, C. L.; Kang, M.; Unwin, P. R. Nanoscale Surface Structure-Activity in Electrochemistry and Electrocatalysis. *J. Am. Chem. Soc.* **2019**, *141*, 2179-2193.

(4) Bentley, C. L.; Kang, M.; Unwin, P. R. Scanning electrochemical cell microscopy: New perspectives on electrode processes in action. *Curr. Opin. Electrochem.* **2017**, *6*, 23-30.

(5) Bentley, C. L.; Edmondson, J.; Meloni, G. N.; Perry, D.; Shkirskiy, V.; Unwin, P. R. Nanoscale Electrochemical Mapping. *Anal. Chem.* **2019**, *91*, 84-108.

(6) Williams, C. G.; Edwards, M. A.; Colley, A. L.; Macpherson, J. V.; Unwin, P. R. Scanning Micropipet Contact Method for High-Resolution Imaging of Electrode Surface Redox Activity. *Anal. Chem.* **2009**, *81*, 2486-2495.

(7) Ebejer, N.; Schnippering, M.; Colburn, A. W.; Edwards, M. A.; Unwin, P. R. Localized High Resolution Electrochemistry and Multifunctional Imaging: Scanning Electrochemical Cell Microscopy. *Anal. Chem.* **2010**, *82*, 9141-9145.

(8) Güell, A. G.; Cuharuc, A. S.; Kim, Y.-R.; Zhang, G.; Tan, S.-y.; Ebejer, N.; Unwin, P. R. Redox-Dependent Spatially Resolved Electrochemistry at Graphene and Graphite Step Edges. *ACS Nano* **2015**, *9*, 3558-3571.

(9) Bentley, C. L.; Kang, M.; Maddar, F. M.; Li, F.; Walker, M.; Zhang, J.; Unwin, P. R. Electrochemical Maps and Movies of the Hydrogen Evolution Reaction on Natural Crystals of Molybdenite (MoS_2): Basal vs. Edge Plane Activity. *Chem. Sci.* **2017**, *8*, 6583-6593.

(10) Bentley, C. L.; Kang, M.; Unwin, P. R. Nanoscale Structure Dynamics within Electrocatalytic Materials. *J. Am. Chem. Soc.* **2017**, *139*, 16813-16821.

(11) Hill, J. W.; Hill, C. M. Directly Mapping Photoelectrochemical Behavior within Individual Transition Metal Dichalcogenide Nanosheets. *Nano Lett.* **2019**, *19*, 5710-5716.

(12) Yule, L. C.; Shkirskiy, V.; Aarons, J.; West, G.; Bentley, C. L.; Shollock, B. A.; Unwin, P. R. Nanoscale Active Sites for the Hydrogen Evolution Reaction on Low Carbon Steel. *J. Phys. Chem. C* **2019**, *123*, 24146-24155.

(13) Aaronson, B. D. B.; Chen, C. H.; Li, H. J.; Koper, M. T. M.; Lai, S. C. S.; Unwin, P. R. Pseudo-Single-Crystal Electrochemistry on Polycrystalline Electrodes: Visualizing Activity at Grains and Grain Boundaries on Platinum for the Fe^{2+}/Fe^{3+} Redox Reaction. *J. Am. Chem. Soc.* **2013**, *135*, 3873-3880.

(14) Mariano, R. G.; McKelvey, K.; White, H. S.; Kanan, M. W. Selective increase in CO_2 electroreduction activity at grain-boundary surface terminations. *Science* **2017**, *358*, 1187-1192.

(15) Wang, Y.; Gordon, E.; Ren, H. Mapping the Nucleation of H2 Bubbles on Polycrystalline Pt via Scanning Electrochemical Cell Microscopy. *J. Phys. Chem. Lett.* **2019**, *10*, 3887-3892.

(16) Tao, B.; Yule, L. C.; Daviddi, E.; Bentley, C. L.; Unwin, P. R. Correlative electrochemistry-microscopy of Li-ion (de)intercalation at series of individual LiMn2O4 particles. *Angew. Chem.-Int. Edit.* **2019**, *58*, 4606-4611.

(17) Tarnev, T.; Barike Aiyappa, H.; Botz, A.; Erichsen, T.; Ernst, A.; Andronescu, C.; Schuhmann, W. SECCM investigation of single ZIF-derived nanocomposite particles as oxygen evolution electrocatalysts in alkaline media. *Angew. Chem.-Int. Edit.* **2019**, *58*, 14265-14269.

(18) Choi, M.; Siepser, N. P.; Jeong, S.; Wang, Y.; Jagdale, G.; Ye, X.; Baker, L. A. Probing Single-Particle Electrocatalytic Activity at Facet-Controlled Gold Nanocrystals. *Nano Lett.* **2020**, *20*, 1233-1239.

(19) McKelvey, K.; O'Connell, M. A.; Unwin, P. R. Meniscus confined fabrication of multidimensional conducting polymer nanostructures with scanning electrochemical cell microscopy (SECCM). *Chem. Commun.* **2013**, *49*, 2986-2988.

(20) Kim, J. T.; Pyo, J.; Seol, S. K.; Je, J. H. Precise Placement of Microbubble Templates at Single Entity Resolution. *ACS Macro Lett.* **2018**, *7*, 1267-1271.

(21) Ornelas, I. M.; Unwin, P. R.; Bentley, C. L. High-Throughput Correlative Electrochemistry−Microscopy at a Transmission Electron Microscopy (TEM) Grid Electrode. *Anal. Chem.* **2019**, *91*, 14854-14859.

(22) Tarnev, T.; Cychy, S.; Andronescu, C.; Muhler, M.; Schuhmann, W.; Chen, Y.-T. A Universal Nano-capillary Based Method of Catalyst Immobilization for Liquid-Cell Transmission Electron Microscopy. *Angew. Chem.-Int. Edit.* **2020**, *59*, 5586-5590.

(23) Zoski, C. G. *Handbook of Electrochemistry*, 1st ed.; Elsevier: Amsterdam, 2007, p 892.

(24) Aaronson, B. D. B.; Lai, S. C. S.; Unwin, P. R. Spatially Resolved Electrochemistry in Ionic Liquids: Surface Structure Effects on

Triiodide Reduction at Platinum Electrodes. *Langmuir* **2014**, *30*, 1915-1919.
(25) Aaronson, B. D. B.; Garoz-Ruiz, J.; Byers, J. C.; Colina, A.; Unwin, P. R. Electrodeposition and Screening of Photoelectrochemical Activity in Conjugated Polymers Using Scanning Electrochemical Cell Microscopy. *Langmuir* **2015**, *31*, 12814-12822.
(26) E, S. P.; Kang, M.; Wilson, P.; Meng, L.; Perry, D.; Basile, A.; Unwin, P. R. High resolution visualization of the redox activity of Li2O2 in non-aqueous media: conformal layer vs. toroid structure. *Chem. Commun.* **2018**, *54*, 3053-3056.
(27) Snowden, M. E.; Dayeh, M.; Payne, N. A.; Gervais, S.; Mauzeroll, J.; Schougaard, S. B. Measurement on isolated lithium iron phosphate particles reveals heterogeneity in material properties distribution. *J. Power Sources* **2016**, *325*, 682-689.
(28) Snowden, M. E.; Güell, A. G.; Lai, S. C. S.; McKelvey, K.; Ebejer, N.; O'Connell, M. A.; Colburn, A. W.; Unwin, P. R. Scanning Electrochemical Cell Microscopy: Theory and Experiment for Quantitative High Resolution Spatially-Resolved Voltammetry and Simultaneous Ion-Conductance Measurements. *Anal. Chem.* **2012**, *84*, 2483-2491.
(29) Bentley, C. L.; Unwin, P. R. Nanoscale electrochemical movies and synchronous topographical mapping of electrocatalytic materials. *Faraday Discuss.* **2018**, *210*, 365-379.
(30) Chen, C.-H.; Jacobse, L.; McKelvey, K.; Lai, S. C. S.; Koper, M. T. M.; Unwin, P. R. Voltammetric Scanning Electrochemical Cell Microscopy: Dynamic Imaging of Hydrazine Electro-oxidation on Platinum Electrodes. *Anal. Chem.* **2015**, *87*, 5782-5789.
(31) Perry, D.; Momotenko, D.; Lazenby, R. A.; Kang, M.; Unwin, P. R. Characterization of Nanopipettes. *Anal. Chem.* **2016**, *88*, 5523-5530.
(32) Sun, P.; Mirkin, M. V. Kinetics of Electron-Transfer Reactions at Nanoelectrodes. *Anal. Chem.* **2006**, *78*, 6526-6534.
(33) Bentley, C. L.; Li, J.; Bond, A. M.; Zhang, J. Mass-Transport and Heterogeneous Electron-Transfer Kinetics Associated with the Ferrocene/Ferrocenium Process in Ionic Liquids. *J. Phys. Chem. C* **2016**, *120*, 16516-16525.
(34) Daviddi, E.; Chen, Z.; Massani, B. B.; Lee, J.; Bentley, C. L.; Unwin, P. R.; Ratcliff, E. L. Nanoscale Visualization and Multiscale Electrochemical Analysis of Conductive Polymer Electrodes. *ACS Nano* **2019**, *13*, 13271-13284.
(35) Linden, D.; Reddy, T. B. *Handbook of Batteries*, 3rd ed.; McGraw-Hill: New York, 2002.
(36) Janisch, J.; Ruff, A.; Speiser, B.; Wolff, C.; Zigelli, J.; Benthin, S.; Feldmann, V.; Mayer, H. A. Consistent diffusion coefficients of ferrocene in some non-aqueous solvents: electrochemical simultaneous determination together with electrode sizes and comparison to pulse-gradient spin-echo NMR results. *J. Solid State Electrochem.* **2011**, *15*, 2083.
(37) Bard, A. J.; Faulkner, L. R. *Electrochemical Methods : Fundamentals and Applications*, 2nd ed.; Wiley: New York, 2001, p 833.
(38) Bentley, C. L.; Perry, D.; Unwin, P. R. Stability and Placement of Ag/AgCl Quasi-Reference Counter Electrodes in Confined Electrochemical Cells. *Anal. Chem.* **2018**, *90*, 7700-7707.
(39) Gerard, M.; Chaubey, A.; Malhotra, B. D. Application of conducting polymers to biosensors. *Biosens. Bioelectron.* **2002**, *17*, 345-359.
(40) Snook, G. A.; Kao, P.; Best, A. S. Conducting-polymer-based supercapacitor devices and electrodes. *J. Power Sources* **2011**, *196*, 1-12.
(41) Li, C.; Bai, H.; Shi, G. Conducting polymer nanomaterials: electrosynthesis and applications. *Chem. Soc. Rev.* **2009**, *38*, 2397-2409.
(42) Zhou, M.; Heinze, J. Electropolymerization of Pyrrole and Electrochemical Study of Polypyrrole. 3. Nature of "Water Effect" in Acetonitrile. *J. Phys. Chem. B* **1999**, *103*, 8451-8457.
(43) Bentley, C. L.; Bond, A. M.; Hollenkamp, A. F.; Mahon, P. J.; Zhang, J. Concentration and Electrode Material Dependence of the Voltammetric Response of Iodide on Platinum, Glassy Carbon and Boron-doped Diamond in the Room Temperature Ionic Liquid 1-ethyl-3-methylimidazolium Bis(Trifluoromethanesulfonyl)imide. *Electrochim. Acta* **2013**, *109*, 554-561.
(44) Bentley, C. L.; Bond, A. M.; Hollenkamp, A. F.; Mahon, P. J.; Zhang, J. Voltammetric Determination of the Iodide/Iodine Formal Potential and Triiodide Stability Constant in Conventional and Ionic Liquid Media. *J. Phys. Chem. C* **2015**, *119*, 22392-22403.
(45) Hagfeldt, A.; Boschloo, G.; Sun, L. C.; Kloo, L.; Pettersson, H. Dye-Sensitized Solar Cells. *Chem. Rev.* **2010**, *110*, 6595-6663.
(46) Tułodziecki, M.; Leverick, G. M.; Amanchukwu, C. V.; Katayama, Y.; Kwabi, D. G.; Bardé, F.; Hammond, P. T.; Shao-Horn, Y. The role of iodide in the formation of lithium hydroxide in lithium–oxygen batteries. *Energy Environ. Sci.* **2017**, *10*, 1828-1842.
(47) Bennett, B.; Chang, J.; Bard, A. J. Mechanism of the Br−/Br2 Redox Reaction on Platinum and Glassy Carbon Electrodes in Nitrobenzene by Cyclic Voltammetry. *Electrochim. Acta* **2016**, *219*, 1-9.
(48) Bentley, C. L.; Bond, A. M.; Hollenkamp, A. F.; Mahon, P. J.; Zhang, J. Electrode Reaction and Mass-Transport Mechanisms Associated with the Iodide/Triiodide Couple in the Ionic Liquid 1-Ethyl-3-methylimidazolium Bis(trifluoromethanesulfonyl)imide. *J. Phys. Chem. C* **2014**, *118*, 29663–29673.
(49) Clavilier, J.; Albalat, R.; Gómez, R.; Orts, J. M.; Feliu, J. M. Displacement of adsorbed iodine on platinum single-crystal electrodes by irreversible adsorption of CO at controlled potential. *J. Electroanal. Chem.* **1993**, *360*, 325-335.

TOC Graphic:

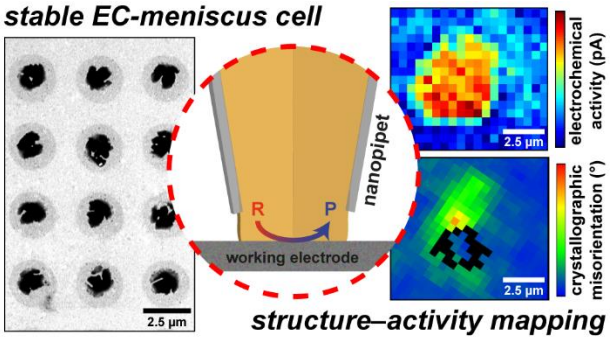
stable EC-meniscus cell
2.5 µm
nanopipet
R
P
working electrode
2.5 µm
2.5 µm
electrochemical activity (pA)
crystallographic misorientation (°)
structure–activity mapping